Journal of Analytical and Applied Pyrolysis 186 (2025) 106948

Contents lists available at ScienceDirect

Journal of Analytical and Applied Pyrolysis

journal homepage: www.elsevier.com/locate/jaap

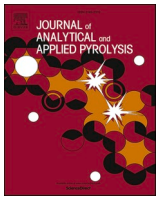

Effect of analcime on hydrocarbon generation for type I kerogen in organic-rich shale by semi-open pyrolysis

Biao Sun [a,b,d], Xiaoping Liu [a,b,*], Xianzheng Zhao [a,b,c], Murray Gingras [d], Qingyong Luo [a,b], Fengming Jin [e], Tian Liu [a,b], Zuxian Hua [a,b], Wendi Peng [a,b], Yu Yuan [a,b]

[a] State Key Laboratory of Petroleum Resources and Engineering, China University of Petroleum (Beijing), Beijing 102249, China
[b] College of Geosciences, China University of Petroleum (Beijing), Beijing 102249, China
[c] China Petroleum Consulting Center, Beijing 100724, China
[d] Department of Earth and Atmospheric Sciences, University of Alberta, Edmonton, AB T6G 2E3, Canada
[e] Dagang Oil Field Company of PetroChina, Tianjin 300280, China

ARTICLE INFO

Keywords:
Analcime
Hydrocarbon generation
Catalytic effects

ABSTRACT

Analcime, a key mineral especially in organic matter-rich sediments, plays a critical role hydrocarbons generation from kerogen. However, its effect on hydrocarbon generation from type I kerogen remains unclear. In this study, semi-open thermal simulation experiments were conducted on lacustrine shale to investigate the relationship between analcime and hydrocarbon generation. Semi-open pyrolysis experiment was performed on type I kerogen in organic-rich shale containing of 15 %, 27 %, and 35 % analcime concentrations across a temperature range of 300 °C to 500 °C. The analcime collected from the study area is sedimentary and diagenetic, characterized as low-silica analcime formed by chemical reactions between clay minerals and sodium-rich alkaline water. Results demonstrate that increasing analcime contents significantly enhances hydrocarbon yields of oil and gas while reducing activation energy, indicating that analcime accelerates hydrocarbon generation from kerogen. However, the durations of hydrocarbon generation appear to decline with increasing analcime contents. Thus, analcime influences hydrocarbon generation by increasing the conversion rate and reducing the generation cycle primarily due to its catalytic effects. Specifically, analcime promotes organic matter decomposition through acidic catalysis and adsorption, establishing an efficient catalytic system.

1. Introduction

Extensive research has focused on how inorganic minerals influence hydrocarbon generation from kerogen during thermal evolution. These minerals can significantly enhance the cracking of complex organic matter, breaking it down into oil and gas. Studies show that clay minerals [1–5], carbonate minerals [6,7], and transition metal elements [8–11] catalyze kerogen's thermal evolution [12–14]. For instance, one study found that increased acidity of kerogen with added minerals ($CaCO_3$ < kaolinite < montmorillonite < alumina) results in a gradual increase in the yield of low molecular weight hydrocarbon components, indicating the existence of inorganic acid catalysis [15]. Additionally, presence of carbonates increased the yield of hydrocarbons and aromatic compounds in oil shale. Alkali metals (Na, K) and alkaline earth metals (Ca, Mg) in carbonate (Mn_nCO_3) exhibit catalytic effects similar to K_2CO_3, Na_2CO_3, $CaCO_3$ and $MgCO_3$, promoting hydroxyl-OH functional group formation and CO_2 generation while reducing CH_4 yield [16]. Despite these insights, the role of analcime in hydrocarbon generation remains a topic of fierce debate [17,18]. Zeolite, a similar mineral, plays a catalytic hydrogenation role and effectively increases oil production, with catalytic effect originated from its surface and interlayer acid groups. The surface acid groups facilitate hydrocarbon cracking, alkanes isomerization, and conversion of olefins to saturated hydrocarbons, while the interlayer acid groups promote dihydroxylation [17]. However, limited research explores the dynamic matching relationship and influencing mechanism of different products of hydrocarbon generation between analcime and organic matter, which constrains the in-depth understanding of the co-evolution of analcime and organic matter.

Zeolite minerals are a class of framework-structured silicate minerals primarily composed of Na, Ca, and Al elements. During diagenetic evolution, their catalytic activity effectively promotes hydrocarbon

* Corresponding author at: State Key Laboratory of Petroleum Resources and Engineering, China University of Petroleum (Beijing), Beijing 102249, China.
E-mail address: liuxiaoping@cup.edu.cn (X. Liu).

https://doi.org/10.1016/j.jaap.2025.106948
Received 4 June 2024; Received in revised form 1 November 2024; Accepted 2 January 2025
Available online 3 January 2025

generation [19–21]. However, zeolite cementation can destroy primary pores and fractures, which reduces the reservoir properties of the rock and inhibits burial compaction during mineral consolidation and diagenesis [22]. Additionally, the dissolution of zeolite increases its porosity, enhancing the reservoir's capacity. Some scholars have suggested that the diagenetic evolution of zeolite may also influence the fracturing properties of shale [23].

As a zeolitic mineral, analcime has the chemical formula $Na[AlSi_2O_6]\cdot H_2O$. It is a low-silicon zeolite with the lowest silicon-aluminum ratio (Si/Al)of any zeolite with a trioctahedral or 24-dihedral crystal structure [24]. The molecular structure of analcime features silicon-oxygen tetrahedrons connected by bridging oxygen, forming either a four-membered or six-membered closed-ring structure in the plane and a cage-like structure in space. Due to its unique molecular sieve structure and catalytic properties, analcime serves as a hydrogen source during the process of hydrocarbon generation from organic matter.

Scientists have identified analcime in the sedimentary strata of numerous basins, with an average content of 14.5 % and a maximum content of 59 % [24–26]. Due to its high compressibility and solubility in reservoir waters analcime plays a significant role in the formation of high-quality oil and gas reservoirs [27]. Consequently, there is both scientific significance and economic value in examining analcime generation from source rocks in lake basins.

Table 1 summarizes the impact of zeolites on hydrocarbon generation as demonstrated in previous studies. These investigations reveal that zeolites exert varying effects on the evolution of hydrocarbon generation from organic matter, influenced by factors such as the type of zeolites, the type of organic matter, the thermal maturity of the organic matter, and experimental methodologies employed [28–31]. Consequently, these findings indicate that zeolites play a significant role in kerogen thermal evolution.

Table 1
Summary of the documented effects zeolites have on hydrocarbon generation from previous studies.

Main Conclusion	Deficiency	Cause of difference
Analcime has a catalytic effect on hydrocarbon generation from source rocks, which can lower the temperature reached during hydrocarbon generation and accelerate the rate of hydrocarbon generation [32].	Catalysis is mainly limited to the contact surface between igneous rocks and source rocks.	1) Form of analcime 2) Ratio of analcime/OM 3) Number of temperatures being studied 4) Experiment equipment/ conditions
On-line ZSM−5 catalytic upgrading of shale oils results in a significant reduction in the overall nitrogen content within the derived shale oils [29].		
The adsorption of F- by ore can be influenced by the amount of analcime organic matter consumption, the size of analcime-modified ore particles, stirring time, and other factors [28].	Limited to the study of water adsorption performance, the adsorption performance of oil and gas was not covered.	
Analcime plays a catalytic role and effectively increases hydrocarbon production. Considering the chemical characteristics of analcime, catalytic effect arises from its B acid and L acid groups. The former can promote hydrocarbon cracking, isomerization of alkanes, and conversion of olefins to saturated hydrocarbons, while the latter can enhance dihydroxylation [31].	There is a single type of analcime and few experimental samples.	
The pyrolysis degradation of polyolefin plastics to aromatic hydrocarbons is catalyzed by zeolites [30].		

Existent within sedimentary rocks, analcime exhibits diverse origins and intricate formation mechanisms. Analcime is classified into four categories based on their genesis types: volcanic material alteration analcime, mineral transformation analcime, hydrothermal analcime and primary analcime [29,33–35].

First, volcanic provenance is formed through the reaction of highly active volcanic glass with a sodium-rich alkaline solution, which is then transformed into the intermediate product alkali zeolite (e.g., clinoptilolite, mordenite). Most zeolite minerals in nature are derived from volcanic materials [36–39]. Conversely, non-volcanic materials originate from the reaction of aluminosilicate gel or aluminosilicate minerals (e.g., montmorillonite, kaolinite, feldspar) with sodium-rich alkaline water, typically found in saline-alkaline lake basin sediments that lack volcanic materials [34]. Third, lacustrine hydrothermal deposition occurs when hydrothermal sedimentary rocks associated with the hydrothermal geyser become active at the bottom of the lake in the continental rift basin [40]. Lastly, direct crystallization occurs in igneous rocks. The Si/Al ratios and mineral structure of analcime vary according to their different origins [23]. Consequently, these factors lead to variations in the catalytic effects on source rocks.

The extensive research on the effects of common minerals on hydrocarbon generation from organic matter has provided a deeper understanding of the influence of analcime on the hydrocarbon generation process (see Table 1). However, the relationship between the amount of analcime and the evolution process of organic matter has not been studied systematically. Therefore, this study conducted semi-open thermal simulation experiments on low-maturity shale samples containing type I kerogen with varying analcime content to evaluate the hydrocarbon generation effect of analcime and its related mechanisms. Low-maturity shale samples were chosen to closely examine the entire thermal maturation process, making this study one of the first comprehensive examinations of the impact of analcime on oil and gas generation, while closely replicating geological conditions.

2. Geological setting

The Bohai Bay Basin is the most significant petroliferous basin found in the Asia-Pacific region, covering an impressive area of 200,000 km^2 (Fig. 1**a**). The Huanghua Depression is a faulted basin formed through a series of rifts and Neogene sag phases. It is located deep within the Bohai Bay Basin, with a general NE-SW orientation. The Huanghua Depression is approximately 250 km long and 50–100 km wide (Fig. 1**b**), covering a total area of about 17,000 km^2 [41]. Following Mesozoic-Cenozoic subsidence and uplift events, the Huanghua Depression developed into the Cangdong Sag (Fig. 1**c**), covering a total area of about 1760 km^2.

The Paleogene strata specifically, the Kongdian, Shahejie, and Dongying formations in Eastern China are considered crucial source rock beds for discovered hydrocarbons. The Kongdian Formation, which is the focus of this study, is the primary hydrocarbon-generating unit and consists of three sub-members (i.e., Ek_3, Ek_2, Ek_1 from bottom to top) (Fig. 1**d**). The sedimentary environment of the Kongdian Formation was a brackish lake. The lithology of the Kongdian Formation predominantly consists of thick dark mudstones interbedded with dolomites and argillaceous dolomites [45].

3. Samples and methods

3.1. Samples

Three samples from the Paleogene Kongdian Formation were collected from the A1 and A2 wells in the Cangdong Sag located in the

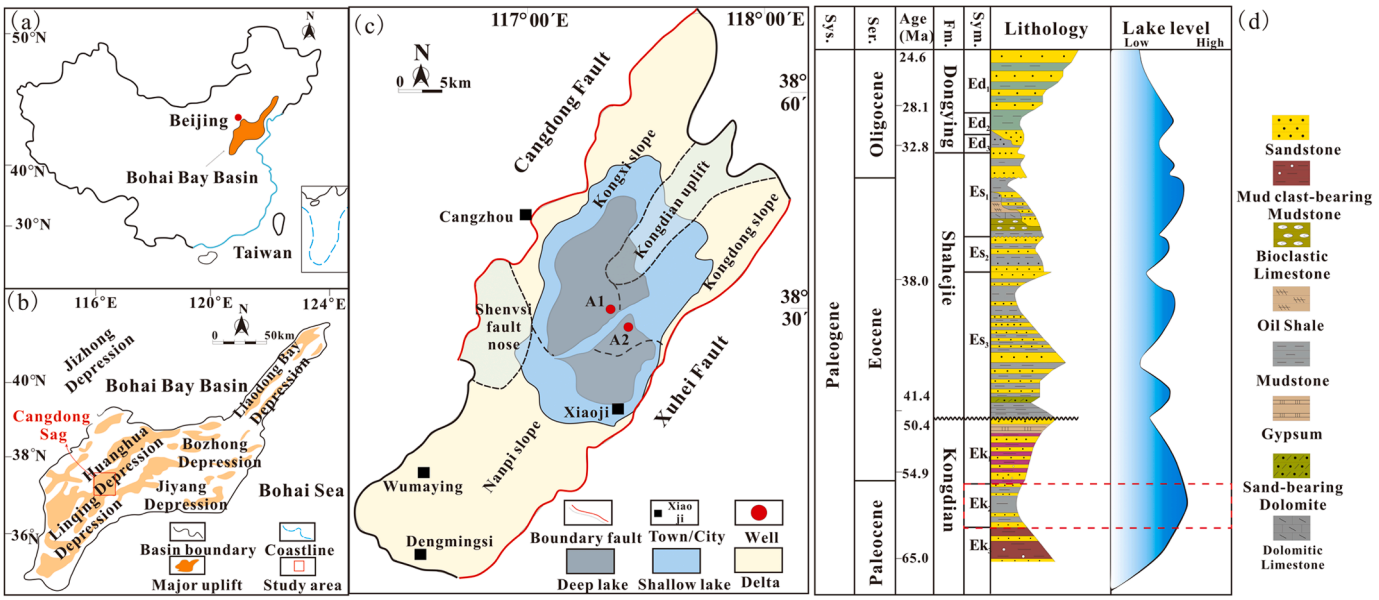

Fig. 1. Location and tectonic units of the study area. (a) Location of Bohai Bay Basin [42]; (b) Division of Basic Structural Units of Bohai Bay Basin[43]; (c) Geological sketch map and the sedimentary facies of the Cangdong Sag showing the location of the sampling well; (d) Paleogene stratigraphic of Huanghua Depression[44].

Bohai Bay Basin (Fig. 1**c**). Thin sections were prepared for each sample, and analyses were conducted to determine the total organic carbon content (TOC) and perform scanning electron microscopy. Additionally, semi-open pyrolysis experiments and kinetic analyses were conducted for the three samples, along with measurements of gas and liquid products. Hydrocarbon generation kinetics were assessed for the three samples, along with the specific operational methodology. To ensure that the hydrocarbon generation and expulsion processes of the samples closely simulated natural geological conditions, columnar samples were also utilized in the thermal simulation experiments. A sample drilling machine was employed to extract six pillars, each with a diameter of 2.5 cm and a length of 2.5 cm, from the same piece of shale to complete the thermal simulation experimental analysis.

3.2. Experiments

3.2.1. X-ray diffraction, thin section analysis, and scanning electron microscopy

The collected samples were ground into a powder using an agate mortar in preparation for the X-ray diffraction (XRD) test. The powder was then analyzed using the Bruker D2 PHASER instrument, allowing for diffractograms to be processed by the Rietveld refinement method [46], which accurately determined mineral compositions of the samples. The acceleration voltage was set to 30 kV, and the electron beam current was 10 mA, while the emission slit and receiving slit were configured to 0.6 mm and 8 mm, respectively.

Regarding the thin section analysis, rock samples were polished or ground to create thin sections. These sections were then examined under both single and orthogonal polarizations at magnification levels ranging from 20–400x.

Shale samples were prepared by polishing them with argon ions using Ilion 697. The polishing process took approximately two hours. The FEI Quanta FEG450 field emission scanning electron microscope was employed to examine the shale samples polished with argon ions using Ilion 697. This examination allowed for the determination of pore properties. It is important to note that the shale samples were polished for about two hours, while the microscope utilized a minimum visible aperture of 2 nm.

3.2.2. Organic petrographic analysis, total organic content and vitrinite reflectance (Ro)

First, the sample was ground into a powder of approximately 0.5 mm. The sample and epoxy resin were placed in a cylindrical mold at a 1:1 ratio and solidified for 24 hours before the light sheet was removed. The light sheet was then examined under a reflective microscope, using white light and fluorescence alternately. The microscopic components of the organic matter were identified based on the characteristics in reflected light, including reflection color, reflection intensity, structural morphology, protrusions, internal reflection, and color, morphology, and intensity under fluorescence. The percentages of microscopic groups such as sapropelite, exinite, vitrinite, and inertinite, were determined by point counting.

To effectively conduct the total organic carbon analysis, the assessed sample size was reduced to a range of 170–200 mesh. After being neutralized with distilled water, inorganic carbon was removed from the samples using a 12.5 % hydrochloric acid solution, and the samples were subsequently dried in an oven at 60–80 °C. The quantity of TOC in the treated powdered samples was then measured.

The vitrinite reflectance of samples was measured using the MSP400 measured, in accordance with the standard ASTM D7708–14 [47].

3.2.3. Semi-open pyrolysis experiments

The thermal simulation experiment utilized a semi-open hydrocarbon generation thermal simulation device developed by the Wuxi Petroleum Geology Research Institute. This device simulates the lithostatic pressure applied to the samples through the upper and lower axes. The cylindrical sample was placed in a stainless-steel autoclave body with a diameter of 3.8 cm and a height of 14.0 cm. Table 2 presents seven temperature points, specifically 300–475 °C for samples 1 and 3, and 300–500 °C for sample 2. To replicate the actual geological conditions experienced at different burial depths, various parameters, including lithostatic pressures and fluid pressures at the hydrocarbon expulsion threshold were set at each temperature point according to specific physical depths. These parameter settings are detailed in Table 2.

Before commencing the experiment, 60 mL of distilled water was injected into the kettle and heated at a rate of 2 °C per minute until the target temperature was reached. During the constant-temperature heating process which took approximately 72 hours, the hydrocarbon

Table 2
Boundary conditions of pyrolysis experiments.

Sample	Depth [m]	Temperature [°C]	Lithostatic pressure [MPa]	Formation pressure [MPa]
PY−300	3116	300	75	31
PY−325	3449	325	83	34
PY−350	3651	350	88	37
PY−375	4538	375	109	45
PY−400	5171	400	124	52
PY−475	5472	475	138	55
PY−500	6000	500	144	60

Note: sample PY number refers to the simulated temperature of the sample in °C.

discharge valve opened when the actual fluid pressure exceeded the initially set fluid pressure of the hydrocarbon expulsion threshold. Generated hydrocarbons were then discharged into a gas-liquid separation tank, which was continuously cooled to below zero for separation, storage, and collection. During the simulation experiment, a cold trap was also utilized to collect the condensate oil discharged with the gas. Dichloromethane was subsequently used to wash the reactor and the inner wall of the pipeline to collect the light oil. The light oil was then combined with the discharged oil of the thermal simulation experiment. After the experiment, dichloromethane was used to extract product from each rock sample, where the oil collected oil represent the retained oil at the corresponding temperature point. The gas products were then analyzed using gas chromatography, while the liquid products were examined through gas chromatography-mass spectrometry (GC-MS). Subsequently, the compounds were grouped into chemical classes.

3.2.4. Gas chromatography and gas chromatography-mass spectrometry (GC-MS)

The Agilent 7890B was used for gas component analysis. The gas vacuum bag injection technique was employed, allowing for the analysis of C_1-C_5 hydrocarbon gases and H_2 in a single injection, thereby improving efficiency. The GC oven temperature was initially set at 30 °C and maintained for 10 minutes, then gradually increased to 180 °C at a rate of 10 °C per minute, and finally held at this temperature for 20–30 minutes.

In the thermal simulation experiment, approximately 20 mg of n-hexane was combined with the collected oil and allowed to precipitate for 24 hours, thereby removing asphaltenes. The remaining components were then adsorbed on an alumina separation column and sequentially eluted with n-hexane, a mixture of dichloromethane and n-hexane (v:v, 1:2), and finally a mixture of dichloromethane and methanol (v:v, 93:7). These solvents were used to elute saturated hydrocarbons, aromatic hydrocarbons, and non-hydrocarbon components, respectively. The saturated hydrocarbon components were subsequently subjected to GC-MS analysis.

The chromatographic column used in this study was the HP-5MS (30 m). The initial temperature was held at 50 °C for one minute, then increased to 100 °C at a rate of 20 °C. It was subsequently raised to 315 °C at a rate of 3 °C per minute and maintained at that temperature for 16 minutes. An Agilent 5977 quadrupole mass spectrometer was employed, operating with a quadrupole temperature of 150 °C. The EI ion source was set to a bombardment energy of 70 eV, with a temperature of 230 °C. The scanning method simultaneously utilized full scan (50–550 amu) and selected ion scanning. The primary selected ions included *m/z* 85, 123, 191, and 217. Relative quantitative analysis of the compounds was performed using the *m/z* 191 mass chromatogram obtained from the selected ion scanning signal, which was manually integrated. This analysis involved determining the peak areas of the related compounds and calculating relevant parameters.

3.2.5. Hydrocarbon generation kinetics

The open system pyrolysis experiments on the three shale samples were conducted using Rock-Eval II. 10 mg of the sample was crushed to approximately 100 mesh and placed in the sample holder for experimentation. The initial temperature of the experiment at 200 °C, and various heating rates were applied. The final temperature was set at 600 °C. The hydrocarbon generation kinetic parameters of the three shale samples were obtained using Kinetics 2015, and the parallel first-order kinetic reaction model was employed to calculate the pre-exponential factor of the shale samples and the corresponding activation energy distribution [48].

$$x(T) = \sum_{i=1}^{N} x_{\infty}(i)\left\{1 - \exp\left[\int_{T_0}^{T} \exp\left(-\frac{E_i}{RT} + \ln A_i - \ln D\right)dT\right]\right\}$$

where, x(T) is the total conversion rate when the reaction reaches temperature T, %; x ∞ (i) is the proportion of reaction x (i) in the total reaction, %; N is the total number of reactions; T_0 is the starting temperature of the reaction, °C; T is the instantaneous temperature of the reaction, °C; E_i is the apparent activation energy of the i-th reaction, kcal/mol; R is the gas constant; A_i is the pre-exponential factor of the i-th reaction, s^{-1}; D is the heating rate, K/s.

4. Results

4.1. Original petrology and geochemical characteristics of unheated samples

The sample information is presented in Table 3. The TOC content across the three samples ranges from 5.51 wt% to 7.87 wt%. Macerals identified in the shale samples include sapropelite, exinite, vitrinite, and inertinite, aligning with findings from previous research [48]. The sapropelite content exceeds 80 % in all three samples. The average pyrolysis peak temperature (T_{max}) value ranges from 435°C to 438.8 °C, and the vitrinite reflectance (Ro) ranges from 0.53 % to 0.57 % indicating low maturity. However, T_{max} and Ro values may be suppressed in kerogen type I [48]. The pyrolysis hydrocarbon generation potential yield (S_1+S_2) range from 39.23 to 62.22 mg HC/ g rock.

The mineralogical analysis results determined by XRD are summarized in Table 4. The mineral composition comprises quartz, feldspar, plagioclase, clay (chlorite, illite, montmorillonite), calcite, ankerite, and analcime. The shale samples predominantly composed of detrital minerals and carbonates with varying analcime content. The carbonate (calcite + ankerite) content ranges from 9 wt% to 25 wt%, averaging 18 wt%; Silicon (quartz+ K-feldspar+ plagioclase) content ranges from 28 wt% to 37 wt%, with an average of 32 wt%; and the clay content ranges from 17 wt% to 24 wt%, averaging 20.7 wt%. Notably, the analcime content varies significantly, ranging from 15 wt% to 35 wt%, with an average of 25.7 wt%. In summary, despite differences in analcime content, the three samples share a similar mineral composition.

4.2. Occurrence characteristics of analcime

Analcime is commonly found in fine-grained lacustrine sediments within the Cenozoic strata of the Bohai Bay Basin, occurring in interlayers alongside organic matter or micritic carbonate. The lamina combinations exhibit variability (Fig. 2**a-b**), with laminae thicknesses ranging from tens to hundreds of microns. During the initial stages of diagenesis, analcime supports the lacustrine shale structure, preventing compaction and retaining some reservoir space (Fig. 2**c**). In the later stages, this analcime occupied space is predominantly filled with oil. Analcime is primarily exists as granular particles, with sizes ranging from 3 μm to 40 μm (Fig. 2**e**), and it frequently coexists with organic matter (Fig. 2**c-f**).

4.3. Total hydrocarbons

Hydrocarbon generation yields both liquid and gas products. The liquid products include retained and discharged oil, while the gas

Table 3
Geochemical characteristics of shale samples.

Sample number	Well	Depth [m]	TOC [wt %]	Kerogen	Tmax [°C]	Ro [%]	S_1 [mg HC/ g rock]	S_2 [mg HC/ g rock]	S_3 [mg HC/ g rock]	PI	HI [mg HC/ g rock]	OI [mg HC/ g rock]	Sapropelite [%]	Exinite [%]	Vitrinite [%]	Inertinite [%]
1	A1	2566.12	5.62	I	437.2	0.53	0.36	39.66	1.05	0.01	705.69	18.68	90	2	6	3
2	A2	2913.76	7.87	I	435	0.55	1.28	60.94	1.21	0.02	774.33	15.37	84	7	7	2
3	A1	2575.47	5.51	I	438.8	0.57	0.29	38.94	0.66	0.01	706.72	11.98	89	4	4	3

products comprise methane (CH_4), heavy hydrocarbon gas (C_2–C_5) and non-hydrocarbon gases such as CO_2, H_2, and N_2. The yield characteristics of generation products obtained from the thermal simulation experiment are presented in Table 5 and Table 6. Experimental results indicate that the three lacustrine shale samples exhibit strong hydrocarbon generation potential, though product types vary depending on the thermal simulation temperature.

As shown in Table 5, the thermal simulation process (i.e., 300–500 °C) can be divided into three stages based on the changes in total hydrocarbon and total oil yield.

Overall, total hydrocarbon and oil yields increase gradually at lower temperatures compared to higher temperatures, such as 300 °C. Specifically, at lower temperatures and low-maturity, total hydrocarbon yields range from 72.37 to 299.76 mg HC/ g rock, while the total oil yields range from 71.2 to 270.76 mg HC/ g rock. As the temperature rises to the range of 325–375 °C, the total hydrocarbon yields increase from 427.28 to 852.46 mg HC/ g rock, and peak total oil yields range from 680.61 to 746.02 mg HC/ g rock. However, as the temperature further increases from 375 to 500 °C, both peak total hydrocarbon and oil yields decline sharply, with values ranging from 402.37 to 816.26 mg HC/ g rock for hydrocarbon and 195.72–731.07 mg HC/ g rock for oil. At this stage, gaseous hydrocarbons are generated in large quantities, leading to increased gas yield, and reduced total hydrocarbon and oil yields owing to polymerization, corresponding to the secondary cracking stage of crude oil.

Regarding total gaseous products, yield changes can be divided into three main stages. First, the total gas yield demonstrates a gradual increase as the simulated temperature rises. In the early stage, kerogen parent material undergoes thermal degradation, resulting primarily in substantial amount of liquid product, while the gaseous yield remains small. In the second stage (325–375 °C), the production of gaseous hydrocarbons increases significantly as the temperature increases, facilitating the increase in gas yield accompanied by a decrease in the liquid hydrocarbon yield, which corresponds to the secondary cracking stage of crude oil. Lastly, in the third stage (375–500 °C), residual organic matter in the source rock is released and converted to gas, leading to a decrease in the retained oil yield. During this stage, gaseous hydrocarbon yield continues to grow, albeit at a diminishing rate.

The pyrolysis yields of total hydrocarbon, total oil, and total gas varied with analcime content. Notably, the peak yield for the 35 % analcime shale was significantly higher than that of the 27 % and 15 % analcime shale. Additionally, the peak temperature for total hydrocarbon products and total oil in the 35 % analcime shale (350 °C) was approximately 25 °C lower than that of other analcime-containing shale samples (375 °C) (Fig. 3).

4.4. Characterisation of gas products

The gaseous products primarily consist of hydrocarbon gases C_1– C_5, and other alkane gases, with their isomeric components (see Table 6), as well as non-hydrocarbon gases, mainly composed of H_2. The variation in CH_4 yield occurs in three distinct stages. Initially, the yield remains relatively stable at temperatures ranging between 300 and 325 °C. It then begins to increase gradually within the temperature range of 325–375 °C. Finally, from 375–500 °C for samples 2 and 3, the yield shows a sharp increase, increasing from 11.28 mg HC/g rock to 48.54 mg HC/g rock in sample 2. The C_2 production displays a gradual increase with temperature, peaking between 5.65 and 14.28 mg HC/g rock. Initially, C_3–C_4 yields progressively increases in sync with rising temperature but later drop rapidly. Furthermore, beyond 400 °C, C_2– C_3 yields from the 35 % analcime shale are significantly higher than those of the other shale samples. The total amount of nC_4 yield for the 35 % analcime shale also increases with rising temperature to 400 °C, surpassing the yield of lower analcime content at corresponding temperatures. Additionally, H_2 production rate increases steadily with rising simulation temperature for all three samples.

Table 4
Mineral composition of shale samples.

Sample number	Quartz [wt%]	K-feldspar [wt%]	Plagioclase [wt%]	Calcite [wt%]	Ankerite [wt%]	Analcime [wt%]	Clay [wt%]	Other [wt%]	Clay		
									Chlorite [wt%]	Illite [wt%]	Illite /montmorillonites [wt%]
1	17	8	6	7	18	15	24	5	3	51	46
2	15	9	4	8	12	27	21	4	3	54	43
3	18	11	8	9	0	35	17	2	2	55	43

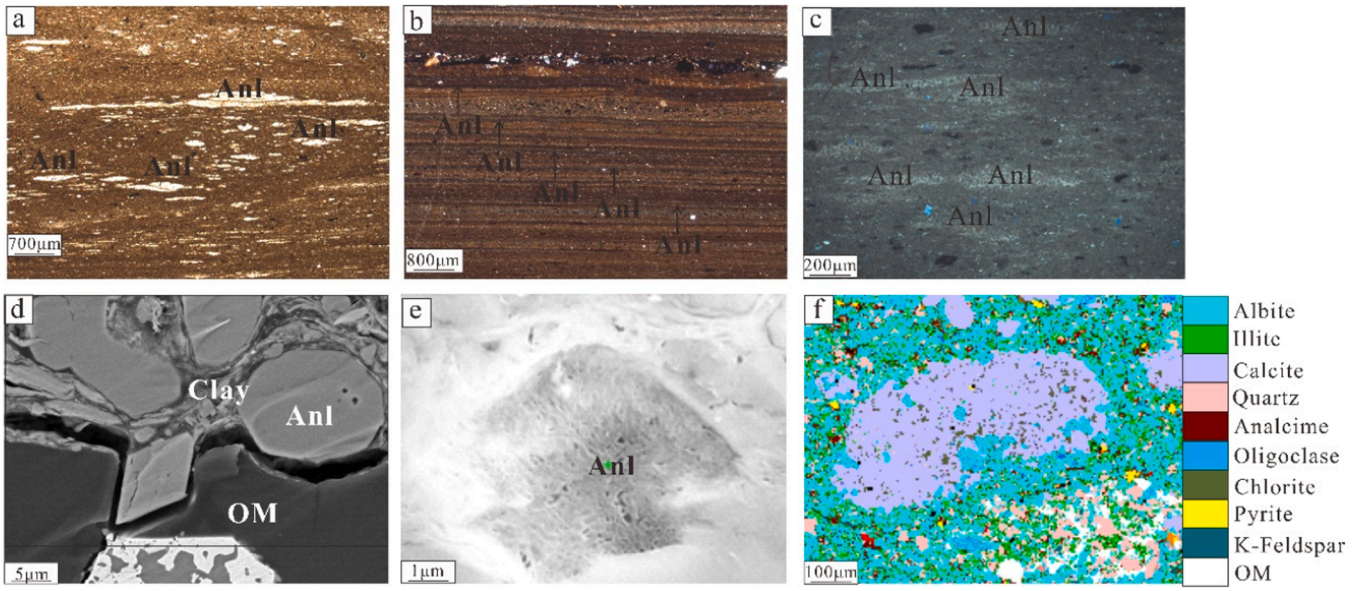

Fig. 2. Occurrence characteristics of analcime in fine-grained sedimentary rocks. (a) Thin section image under plane polarized light shows the fusiform distribution characteristics of analcime, Well A1, 2566.12 m; (b) Thin section image under plane polarized light shows the laminae distribution characteristics of analcime, Well A1, 2575.47 m; (c) Thin sections under fluorescence shows analcime-filled space occupied by oil, Well A1, 2566.12 m; (d) SEM image shows shale comprised clay, analcime (Anl), and organic matter (OM), Well A1, 2575.47 m; (e) SEM image shows Subhedral globules of analcime, Well A1, 2575.47 m; (f) The QEMSCAN image shows organic matter, in which fractures are partially filled with analcime, Well A1, 2566.12 m.

Table 5
Hydrocarbon products from the pyrolysis experiments on shales with different analcime contents.

Sample number	Temperature [°C]	Ro [%]	Discharged oil [mg HC/ g rock]	Retained oil [mg HC/ g rock]	Total oil [mg HC/ g rock]	Total gas [mg HC/ g rock]	Total hydrocarbon products [mg HC/ g rock]
1	PY−300	0.61	9.36	205.08	214.44	3.04	217.48
	PY−325	0.74	21.66	204.71	226.37	9.13	235.50
	PY−350	1.01	121.68	275.00	396.68	30.60	427.28
	PY−375	1.18	190.98	489.63	680.61	29.99	710.60
	PY−400	1.41	189.74	46.17	235.91	182.80	418.72
	PY−475	2.35	190.22	7.98	198.20	204.17	402.37
2	PY−300	0.60	5.41	65.79	71.20	1.17	72.37
	PY−325	0.75	14.02	153.07	167.09	4.89	171.97
	PY−350	1.00	38.17	500.46	538.63	29.42	568.04
	PY−375	1.21	449.49	281.58	731.07	52.37	783.44
	PY−400	1.42	382.15	54.08	436.23	121.80	558.03
	PY−500	2.50	189.46	6.26	195.72	394.94	590.66
3	PY−300	0.63	16.79	117.59	134.38	14.48	148.86
	PY−325	0.73	38.11	232.66	270.76	29.00	299.76
	PY−350	0.98	375.18	370.84	746.02	106.44	852.46
	PY−375	1.19	351.08	243.91	594.99	175.45	770.44
	PY−400	1.44	254.99	58.51	313.50	450.18	763.68
	PY−475	2.37	219.54	11.30	230.84	585.42	816.26

4.5. Molecular biomarkers analysis

The derived carbon number distribution range of n-alkanes observed in the original sample predominantly spans C_{13}–C_{32}, with a single-peak pattern. The primary peak carbon numbers are C_{17} or C_{21}, showing a notable preference for odd-numbered carbons. The ΣC_{21}–ΣC_{22}+ ratio ranges from 0.92 at 350 °C for analcime-15 % to 6.09 at 325 °C for the analcime-27 % (Fig. 4**a**), with the highest ratio of 6.09 observed at 325 °C for and the lowest ratio of approximately 1.09 at 500 °C for the analcime-27 %.

Table 6
Amounts of different gases produced during pyrolysis of shales of different analcime contents.

Sample number	Temperature [°C]	C_1 [mg HC/ g rock]	C_2H_6 [mg HC/ g rock]	C_2H_4 [mg HC/ g rock]	C_3H_8 [mg HC/ g rock]	C_3H_6 [mg HC/ g rock]	iC_4 [mg HC/ g rock]	nC_4 [mg HC/ g rock]	C_4H_8 [mg HC/ g rock]	iC_5 [mg HC/ g rock]	nC_5 [mg HC/ g rock]	H_2 [mg HC/ g rock]
1	PY−300	3.34	0.50	0.00	0.45	0.00	0.08	0.17	0.00	0.06	0.17	0.60
	PY−325	3.94	0.97	0.00	0.69	0.00	0.11	0.30	0.00	0.08	0.23	1.11
	PY−350	7.58	2.19	0.00	1.53	0.02	0.23	0.72	0.00	0.16	0.49	1.38
	PY−375	10.85	3.37	0.00	2.40	0.01	0.33	1.14	0.00	0.23	0.62	1.04
	PY−400	14.98	7.03	0.00	5.63	0.04	0.71	2.77	0.02	0.49	1.29	1.66
	PY−475	20.66	5.65	0.00	2.25	0.00	0.19	0.09	0.00	0.00	0.03	7.76
2	PY−300	1.16	0.22	0.00	0.13	0.00	0.04	0.05	0.00	0.03	0.03	1.49
	PY−325	2.95	0.85	0.00	0.46	0.00	0.10	0.18	0.00	0.06	0.08	1.69
	PY−350	22.14	4.22	0.00	1.43	0.00	0.25	0.36	0.00	0.15	0.11	7.24
	PY−375	11.28	4.47	0.00	3.01	0.04	0.39	1.37	0.01	0.25	0.58	2.09
	PY−400	18.20	9.87	0.00	7.56	0.12	0.73	2.85	0.03	0.26	0.62	2.76
	PY−500	48.54	14.28	0.00	1.78	0.04	0.09	0.20	0.00	0.02	0.07	11.65
3	PY−300	4.54	1.01	0.00	1.25	0.03	0.16	0.47	0.00	0.13	0.47	2.62
	PY−325	8.20	2.62	0.00	1.96	0.03	0.29	0.84	0.02	0.21	0.68	2.35
	PY−350	13.91	5.57	0.00	4.07	0.00	0.64	1.93	0.00	0.48	1.33	2.19
	PY−375	13.82	5.87	0.00	4.54	0.04	0.58	2.33	0.03	0.46	1.37	3.17
	PY−400	16.47	9.08	0.00	7.97	0.09	0.94	4.02	0.05	0.68	1.92	3.26
	PY−475	35.47	13.41	0.00	5.78	0.00	0.47	0.32	0.00	0.00	0.07	9.11

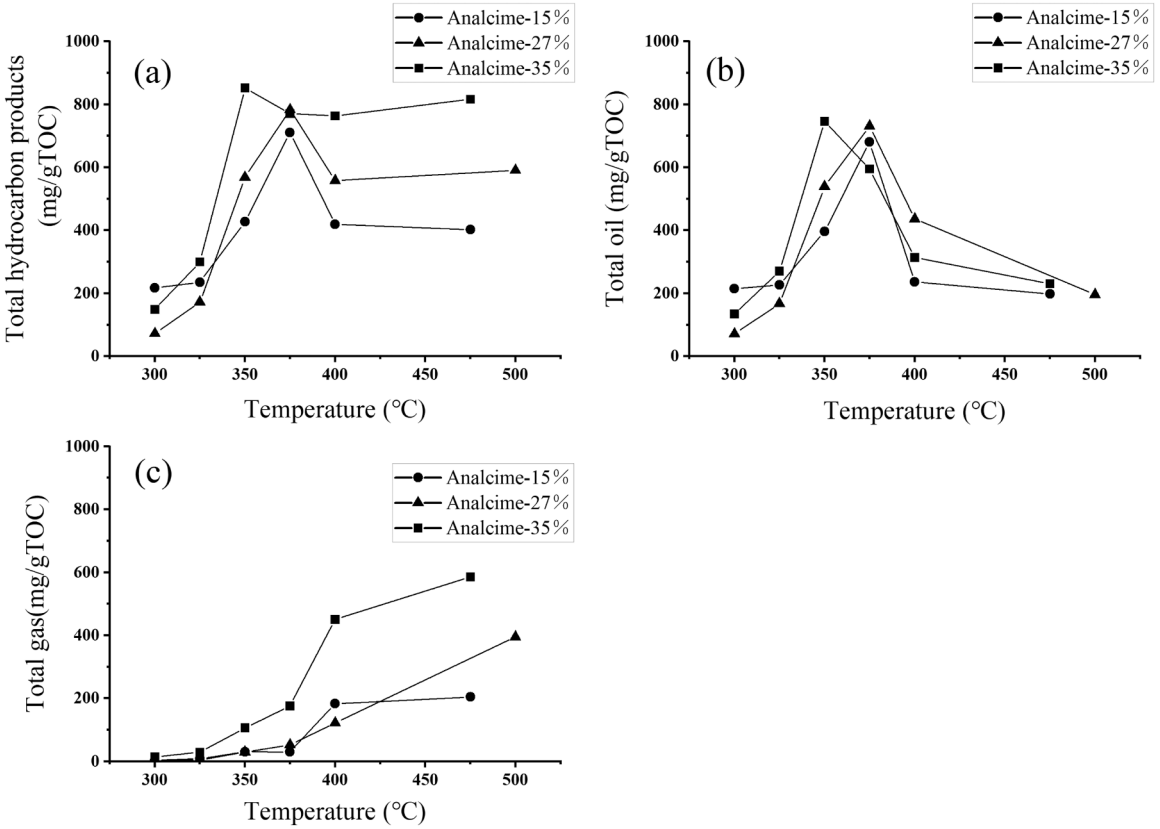

Fig. 3. Yields of total hydrocarbon products (a), total oil (b), total gas (c) in the pyrolysis experiment.

During thermal simulation process (Ro = 0.60 %–2.50 %), the carbon number distribution range of the n-alkanes in the thermal simulation product remains consistently at between C_{13}–C_{32}, with C_{17} as the primary peak carbon.

Among these indicators, the odd-even dominance index (OEP) is a commonly utilized maturity parameter (Fig. 4**b**). At higher maturity stage, a decrease in the OEP ratio was observed [49–51]. The OEP values of the samples ranged from 1.03–1.29 at 300 °C, with a decline occurring as the temperature increased, consistent with the maturing process. Notably, while a decrease was observed up to 400 °C, temperatures exceeding this threshold resulted in minimal change, containing 27 % and 15 % analcime change noted for all three samples. The isoprenoid alkane series compounds exhibit greater thermal stability than n-alkanes, and is therefore predominantly retained during the degradation [52].

The primary isoprenoid products identified in this thermal simulation experiment were phytane (Ph) and pristane (Pr). As the thermal simulation progressed, Ph underwent demethylation, converting to pristane (Pr). The Pr/C_{17}–Ph/C_{18} ratios effectively indicate the degree of thermal evolution of organic matter, decreasing as thermal simulation temperatures increases (Fig. 4**c** and **d**). This reduction, corresponding to a transition from Ro = 0.60 % to Ro = 2.50 %, reflects the structural

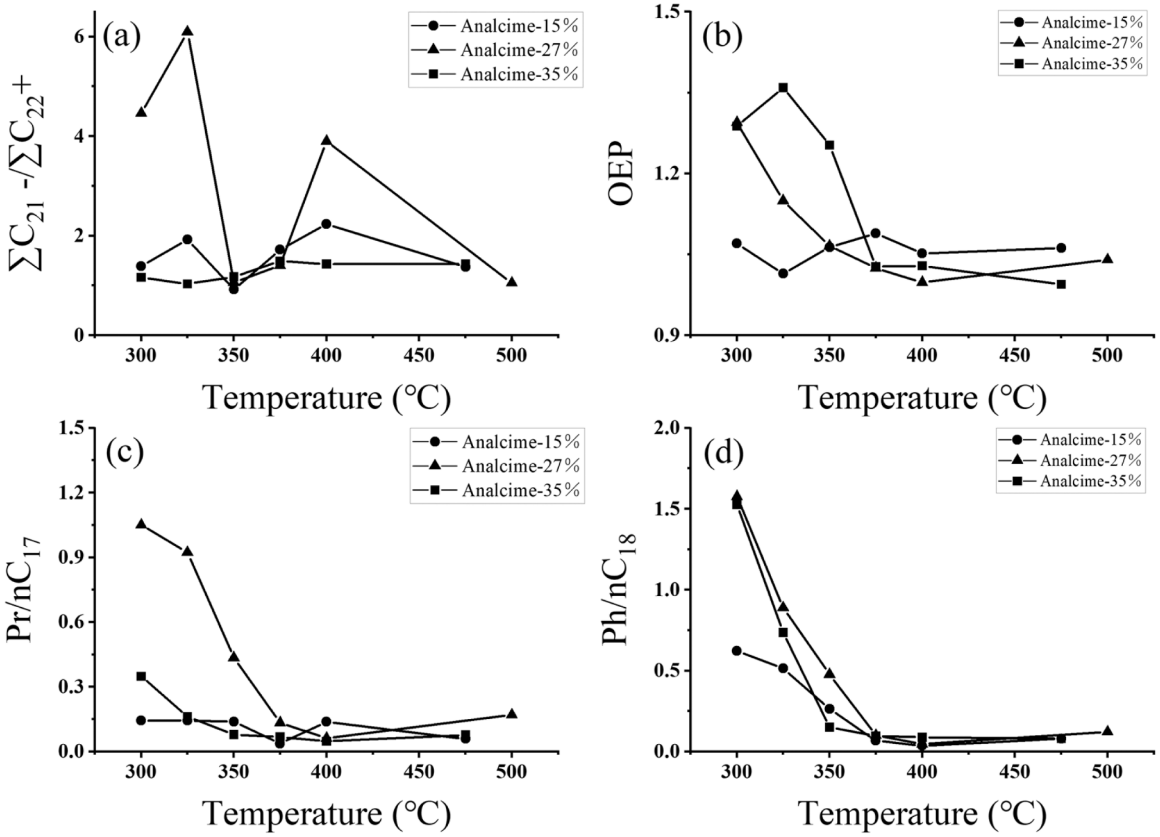

Fig. 4. Aliphatic hydrocarbon molecular composition characteristics of the hydrocarbons.

hydrocarbons breakdown and the ratios diminish. Although yields in the three samples were similar, the 35 % analcime shale exhibited lower maturity compared to the 15 % analcime shale.

5. Discussion

5.1. Formation mechanisms of analcime

The analcime content of the shale samples analyzed was 15 %, 27 %, and 35 %, with an average content of 25 % (Table 3), indicating relatively high analcime content. These values align well with analcime content results from rock-thin section observations and XRD analysis on samples from the same geographical region [26]. The analysis also revealed that the authigenic analcime in the study area, Bohai Bay Basin is primarily formed through the chemical reaction of clay minerals and sodium-rich alkaline water. This conclusion is supported by a significant negative correlation between the analcime and the clay minerals content, with a Se value of 0.562 (Fig. 5), suggesting that clay minerals are the primary source of analcime formation, consistent with the observed average clay mineral content of 21 %. Additionally, volcanic activity in the study area was limited, with no evidence of other types of analcime. The comprehensive analysis strongly indicates that the sole source of analcime in the study area is due to mineral transformation [26].

Analcime typically forms under the influence of strongly alkaline sedimentary waters or formation fluids that are rich in Na^+. This Na^+ can be converted into analcime through exchanges with ions such as Mg^{2+}, Ca^{2+}, K^+, clay minerals, plagioclase, and other minerals. This type of analcime generally occurs during low-temperature stages, predominantly from the syn-diagenetic stage to early diagenetic stage. Analcime formed under these conditions is typically scattered in distribution, fills voids in the rock, and exhibits low euhedral crystallinity. The Si/Al ratio of this analcime ranges from 2.00–2.28, characteristic of low-silicon analcime [53–55].

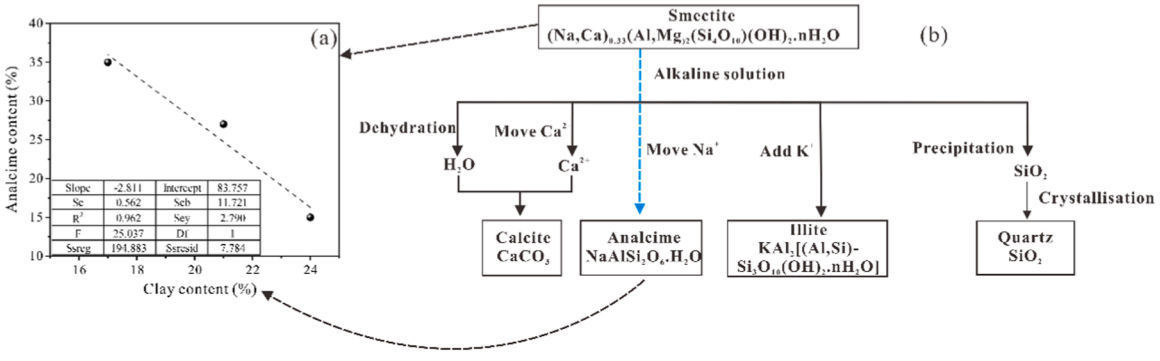

Fig. 5. The correlation between analcime and clay contents in the study (a). Transformations of minerals in fine grained rocks occurring in the study area (b).

5.2. The effect of analcime on the activation energy of hydrocarbon generation

The generation of oil from source rocks is a thermal degradation process of kerogen, occurring over geological time scales. Assuming that the pre-exponential factor A and activation energy E, which are kinetic parameters obtained under high-temperature and rapid conditions in the laboratory, are consistent with those governing the evolution of organic matter over geological period, the laboratory -derived kinetic parameters can be applied to these calculations.

The range and main frequency of the activation energy distribution serve as indicators to differentiate hydrocarbon generation ability among samples. Specifically, a broader activation energy distribution range corresponds to a prolonged hydrocarbon generation period for organic matter and indicate a wide variety of reaction types. Conversely, a narrow activation energy distribution range indicates a shorter hydrocarbon generation period for organic matter.

The magnitude of the peak activation energy indicates the level of difficulty involved in hydrocarbon generation. Thus, a lower highest-frequency activation energy suggests a lower temperature threshold for hydrocarbon generation, resulting in earlier generation. Conversely, a larger highest-frequency activation energy signifies a higher temperature threshold, leading to a relatively delayed onset of hydrocarbon generation [32].

Fig. 6 shows that the pyrolysis hydrocarbon generation kinetic parameters show significant variability for shale samples with different analcime content in the study area. Samples 1, 2, and 3 exhibit average activation energies of 344 kJ/mol, 282 kJ/mol, and 235 kJ/mol, respectively. Sample 1 is characterized by a dispersed activation energy distribution, with the main activation energy range extending from 162–750 kJ/mol (Fig. 6**a**). Sample 2 shows an activation energy distribution from 153–650 kJ/mol (Fig. 6**c**). In contrast, sample 3 has a concentrated activation energy distribution, ranging from 150–675 kJ/mol (Fig. 6**e**).

Upon examining the conversion curves, the hydrocarbon generation characteristics of the three shale samples can be distinctly identified (Fig. 6**b, d, f**). Based on the actual geological conditions, the activation energy range corresponding to a conversion rate of 10–90 % is used as the hydrocarbon generation range [56]. For sample 1, the simulated activation energy for hydrocarbon generation starts at 230 kJ/mol progressing to 630 kJ/mol by the end, indicating hydrocarbon generation occurs over a relatively broad activation energy range (approximately 400 kJ/mol) (Fig. 6**b**). For sample 2, the initial simulated activation energy of hydrocarbon generation was 220 kJ/mol, increasing to 500 kJ/mol, indicating comparatively narrower activation energy range (approximately 280 kJ/mol) for hydrocarbon generation (Fig. 6**d**). Finally, for sample 3, the simulated activation energy of hydrocarbon generation was 195 kJ/mol at the outset and 320 kJ/mol at the conclusion, indicating that hydrocarbon generation for this sample occurs within a relatively narrow activation energy range (approximately 125 kJ/mol) (Fig. 6**f**).

A comparison of the hydrocarbon generation conversion curves for the three shale samples reveals that sample 1 has a hydrocarbon generation threshold of 162 kJ/mol, with a slow conversion rate and a long

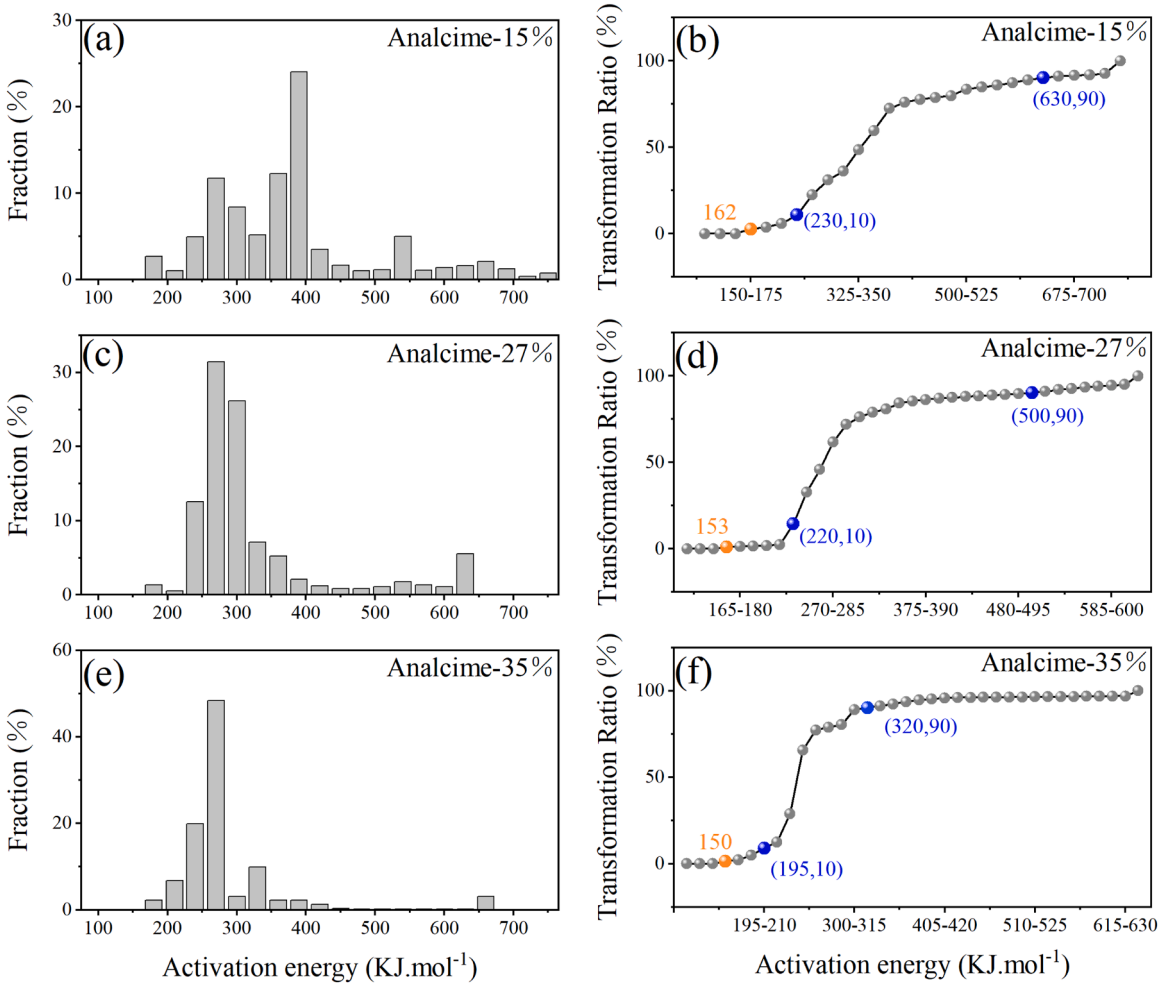

Fig. 6. Kinetic parameters and hydrocarbon generation transformation rate of hydrocarbon generation of analcime-different contents samples.

hydrocarbon generation period. Sample 2 has a hydrocarbon generation threshold of 153 kJ/mol, while sample 3, with lowest threshold of 150 kJ/mol, exhibits the fastest conversion rate and the shortest hydrocarbon generation period.

These findings indicate that as analcime content increases, the hydrocarbon generation threshold decreases, the conversion rate increases, and the duration of hydrocarbon generation diminishes. Additionally, these low-silica analcime minerals possess large pore spaces capable of effectively adsorbing high-molecular weight organic compounds. An efficient catalytic system can be established from the analcime and the organic matter retained in the larger pores, significantly enhancing the conversion efficiency of organic matters. Thus, with higher low-silica analcime content, the catalytic activity becomes more pronounced, resulting in narrower hydrocarbon generation range, which greatly improves the conversion efficiency of organic matter.

There was a significant positive correlation between analcime content and total oil (Fig. 7**a**), gas (Fig. 7**b**), and total hydrocarbon product yields (Fig. 7**c**). These findings align with previous studies indicating that hydrocarbon generation improves significantly with the presence of analcime [17,18]. Moreover, a significant negative correlation exists between analcime content and average activation energy (Fig. 7**d**). Therefore, it is proposed that analcime transformed from clay exhibits strong catalytic ability by reducing the average activation energies, thereby accelerating the hydrocarbon generation process. Compared to sample 1, sample 3 shows increased total hydrocarbon, total oil, and total gas yields by 51.4 %, 17.3 %, and 196.0 %, respectively. Additionally, $NaHCO_3$ and K_2CO_3 enhanced the yield of C_1–C_5 hydrocarbons by 200 % and 100 %, respectively [57], while $CaCO_3$ showed no obvious catalytic effect on hydrocarbon yield[58]. This comparison demonstrates that analcime is superior to K_2CO_3 and $CaCO_3$ regarding catalytic effects in hydrocarbon generation.

5.3. Catalytic effects of analcime

The catalytic mechanism of analcime is primarily linked to Brønsted and Lewis acid groups, which typically give rise to two catalytic hydrocarbon generation mechanisms: the free radical catalysis mechanism and the carbon ion mechanism (Fig. 8) [59,60]. The free radical catalysis mechanism involves the decarboxylation of organic matter, during which analcime, acting as a Lewis acid, accepts an electron from the organic matter. Subsequently, the carboxylic acid loses CO_2, leading to the formation of free radicals that undergo rearrangement reactions, causing the breakage of C-C bonds. This process results in the generation of free hydrocarbons with shorter chain lengths, as illustrated in their reaction formula:

$$CH_3(CH_2)_nCOOH \longrightarrow CH_3(CH_2)_{n-1}\cdot CH_2 + CO_2 + H$$

A parameter for the carbon ion mechanism stipulates that during the thermal cracking reaction of organic matter, analcime must act as a Brønsted acid to provide protons (H^+) for the adsorbed organic matter. Protons (H^+) are generated from the dissociation of adsorbed water and interlayer water molecules, along with exchangeable cations, primarily via the carbocation-forming transition states, as detailed below.

$$n\left[M(H_2O)_x\right] \xrightarrow{k} n\left[M(H_2O)_{x-1}\cdot OH\right] + nH^+$$

In the above formula, M denotes the exchangeable cation, x represents the number of water molecules directly coordinated with M, n indicates the number of exchangeable cations; and k signifies the dissociation constant of interlayer water.

Low-silica analcime exhibits high acid content, high acid strength, and robust catalytic activity All of which effectively promote and facilitate the cracking reaction of hydrocarbon substances. Additionally, the presence of large pores in low-silica analcime facilitates the adsorption of high-molecular organic matter. The interaction between analcime and the adsorbed organic matter in the pores form an efficient

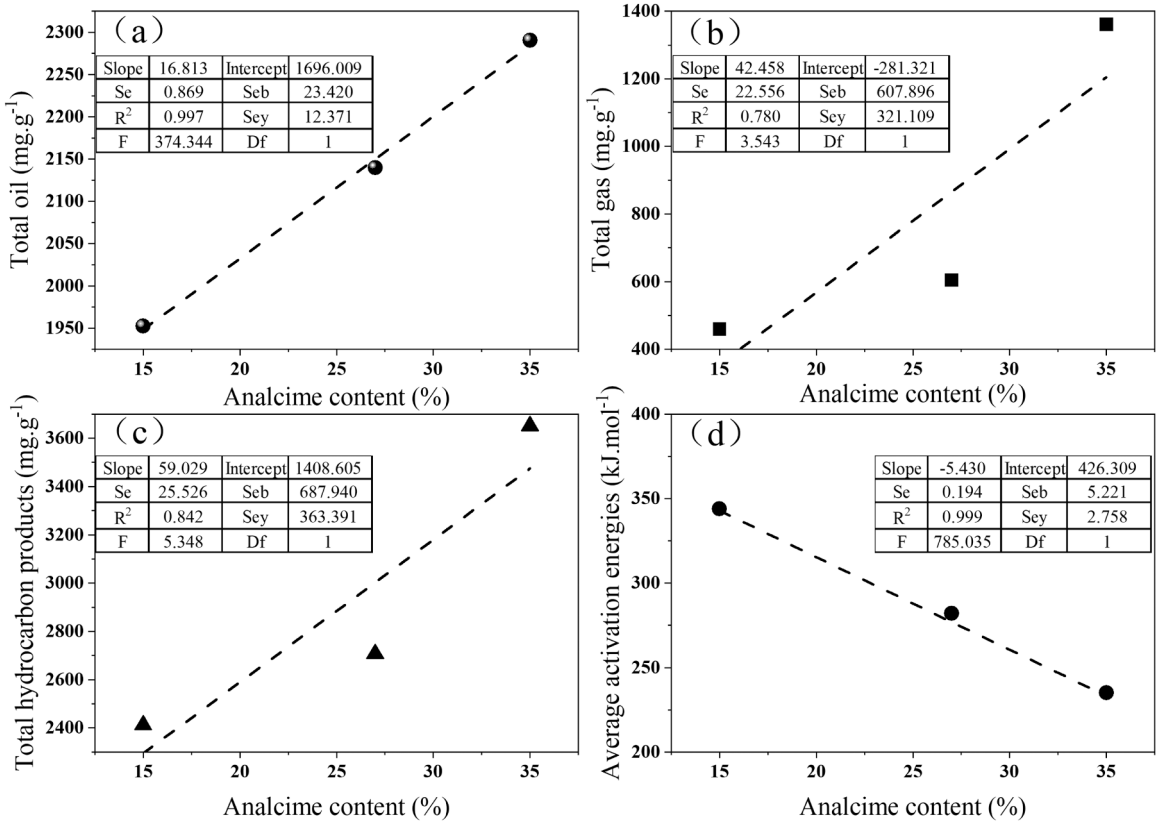

Fig. 7. The correlation between analcime contents and Total oil (a), Total gas (b), Total hydrocarbon products (c), and Average activation energies (d) in the study.

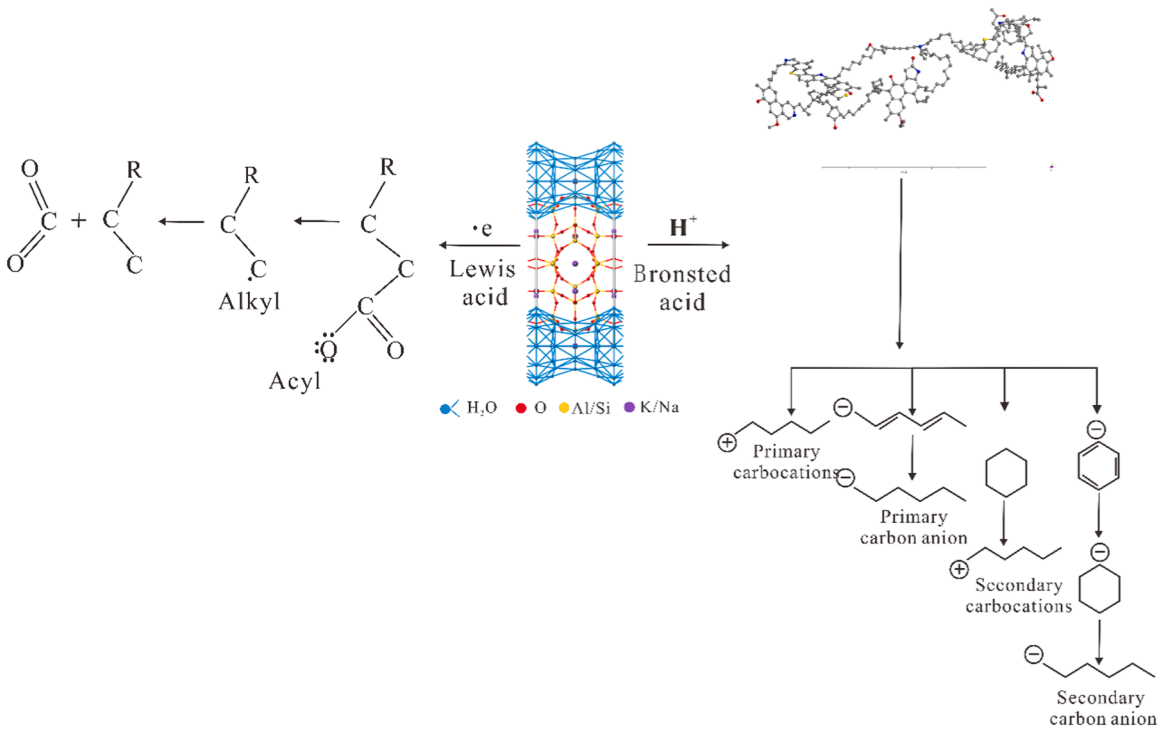

Fig. 8. Mechanisms of analcime catalysis of hydrocarbon generation.

catalytic system, significantly enhancing the conversion efficiency of organic matter [61].

However, the deactivation rate of low-silica analcime is considerable due to two primary factors [60,62]. First, elevated temperatures can hinder the catalytic activity of higher analcime concentrations, potentially compromising their effectiveness. Low-silica analcime has weak thermal stability; thus, during high-temperature catalytic processes, the internal structure of analcime is susceptible to collapse, impairing its catalytic performance. Furthermore, low-silica analcime is highly acidic, which stimulates vigorous reactions with organic matter and generates a substantial amount of coke precursor, obstructing the acidic centers of the catalyst and hindering its catalytic effectiveness.

6. Conclusions

Analcime is an important mineral commonly found in lacustrine sediments. Research on the effects of analcime on hydrocarbon generation has sparked controversy. To address this gap, we conducted semi-open pyrolysis experiments on shale samples with varying levels of analcime at different temperatures to investigate its effects on total oil and total gas production. This study indicate that analcime forms from the reaction of smectite and sodium-rich alkaline water in the study area, consistent with previous studies [26]. Overall, the yields of total hydrocarbon products, total oil, and total gas increased owing to the influence of analcime. Analcime accelerates hydrocarbon generation, shifting the maximum yield 25 °C lower, likely attributed to the formation of an efficient catalytic system between analcime and the organic matter adsorbed in the pores, which significantly improves the conversion efficiency of organic matter. This research provides relevant geological examples that analyze the effect of analcime on hydrocarbon generation. However, attempts to utilize molecular dynamics simulations were still unable to elucidate the catalytic mechanisms of analcime on hydrocarbon generation from a micro to nanoscale perspective. These dynamics may further influence hydrocarbon generation capacity during thermal maturation, making this a key area for future research.

Author statement

All authors disclosed no relevant relationships.

CRediT authorship contribution statement

Biao Sun: Writing – original draft, Visualization, Methodology, Investigation, Data curation, Conceptualization. **Xianzheng Zhao:** Writing – review & editing, Resources. **Xiaoping Liu:** Writing – review & editing, Funding acquisition. **Zuxian Hua:** Methodology, Investigation. **Tian Liu:** Visualization, Software. **Yu Yuan:** Visualization. **Wendi Peng:** Methodology. **Murray Gingras:** Writing – original draft. **Fengming Jin:** Resources. **Qingyong Luo:** Writing – review & editing.

Declaration of Competing Interest

The authors declare that they have no known competing financial interests or personal relationships that could have appeared to influence the work reported in this paper.

Acknowledgments

This work was financially supported by the National Natural Science Foundation of China (Grant No. 42072150) and we thank the sponsors of this project. We acknowledge Dr. Haoquan Hu and four anonymous reviewers for their valuable comments and suggestions, which greatly improved the manuscript of an earlier version.

Data Availability

Data will be made available on request.

References

[1] H.M. Rahman, M. Kennedy, S. Löhr, D.N. Dewhurst, N. Sherwood, S. Yang, B. Horsfield, The influence of shale depositional fabric on the kinetics of hydrocarbon generation through control of mineral surface contact area on clay

catalysis, Geochim. Cosmochim. Acta 220 (2018) 429–448, https://doi.org/10.1016/j.gca.2017.10.012.
[2] M. He, Z. Wang, M.J. Moldowan, K. Peters, Insights into catalytic effects of clay minerals on hydrocarbon composition of generated liquid products during oil cracking from laboratory pyrolysis experiments, Org. Geochem. 163 (2022) 104331, https://doi.org/10.1016/j.orggeochem.2021.104331.
[3] T. Zhao, S. Xu, F. Hao, Differential adsorption of clay minerals: implications for organic matter enrichment, Earth-Sci. Rev. 246 (2023) 104598, https://doi.org/10.1016/j.earscirev.2023.104598.
[4] J. Cai, J. Du, M. Song, T. Lei, X. Wang, Y. Li, Control of clay mineral properties on hydrocarbon generation of organo-clay complexes: evidence from high-temperature pyrolysis experiments, Appl. Clay Sci. 216 (2022) 106368, https://doi.org/10.1016/j.clay.2021.106368.
[5] V. Milesi, A. Prinzhofer, F. Guyot, M. Benedetti, R. Rodrigues, Contribution of siderite-water interaction for the unconventional generation of hydrocarbon gases in the Solimões basin, north-west Brazil, Mar. Pet. Geol. 71 (2016) 168–182, https://doi.org/10.1016/j.marpetgeo.2015.12.022.
[6] Y. Pan, Z. Huang, T. Li, X. Xu, X. Guo, R. Wang, H. Zheng, W. Zhang, Study on the origin and hydrocarbon generation potential of lacustrine organic-rich dolomite affected by volcanism: a case study of Lucaogou Formation in the Malang Sag, Santanghu Basin, Western China, Mar. Pet. Geol. 141 (2022) 105699, https://doi.org/10.1016/j.marpetgeo.2022.105699.
[7] J. Zhang, J. Cao, W. Hu, D. Zhi, X. Guo, B. Bian, Insights into Carboniferous subduction-related petroleum systems in the Central Asian Orogenic Belt (CAOB) from hydrocarbons in vein calcite cements, West Junggar, northwest China, Mar. Pet. Geol. 124 (2021) 104796, https://doi.org/10.1016/j.marpetgeo.2020.104796.
[8] C. Zhang, D. Liu, Q. Liu, S. Jiang, X. Wang, Y. Wang, C. Ma, A. Wu, K. Zhang, Y. Ma, Magmatism and hydrocarbon accumulation in sedimentary basins: a review, Earth-Sci. Rev. 244 (2023) 104531, https://doi.org/10.1016/j.earscirev.2023.104531.
[9] Y. Li, W. Yang, Q. Wang, Y. Song, Z. Jiang, L. Guo, Y. Zhang, J. Wang, Influence of the actively migrated diagenetic elements on the hydrocarbon generation potential in tuffaceous shale, Fuel 256 (2019) 115795, https://doi.org/10.1016/j.fuel.2019.115795.
[10] C.A.S. Teixeira, R.M.S. Bello, N.S. Almeida, A. Pestilho, S. Brochsztain, T.B. de Queiroz, L.S. Andrade, D.F.G. Júnior, A.O. Sawakuchi, Hydrocarbon generation in the Permian Irati organic-rich shales under the influence of the early cretaceous Paraná Large Igneous Province, Mar. Pet. Geol. 117 (2020) 104410, https://doi.org/10.1016/j.marpetgeo.2020.104410.
[11] A.N. Mikhailova, G.P. Kayukova, G.A. Batalin, V.M. Babayev, A.V. Vakhin, Comparative influence's research of the compound of metals carboxylates on the generation and composition of hydrocarbons from Domanic deposits at steam-thermal effect in CO2 environment, J. Pet. Sci. Eng. 186 (2020) 106699, https://doi.org/10.1016/j.petrol.2019.106699.
[12] L.O. Lawal, A.R. Adebayo, M. Mahmoud, A. Sultan, S. Patil, Thermal maturation, mineral catalysis, and gas generation kinetics of carbonate source rock, J. Nat. Gas. Sci. Eng. 92 (2021) 104003, https://doi.org/10.1016/j.jngse.2021.104003.
[13] X. Ma, G. Zheng, W. Sajjad, W. Xu, Q. Fan, J. Zheng, Y. Xia, Influence of minerals and iron on natural gases generation during pyrolysis of type-III kerogen, Mar. Pet. Geol. 89 (2018) 216–224, https://doi.org/10.1016/j.marpetgeo.2017.01.012.
[14] M. Yu, G. Gao, W.-Y. Ma, M. Liu, N. Zhou, Y.-J. Zhang, D. He, K.-T. Fan, L.-L.-B. Guo, J. Li, Hydrocarbon generation differences of shales composed of green algal and cyanobacteria: a case study of Mesozoic and Cenozoic saline lacustrine shales in Junggar Basin, NW China, Pet. Sci. (2023), https://doi.org/10.1016/j.petsci.2023.08.023.
[15] W.E. Robinson, Isolation Procedures for Kerogens and Associated Soluble Organic Materials, in: G. Eglinton, M.T.J. Murphy (Eds.), BT - Organic Geochemistry: Methods and Results, Springer Berlin Heidelberg, Berlin, Heidelberg, 1969, pp. 181–195, https://doi.org/10.1007/978-3-642-87734-6_7.
[16] W. Qing, Z. Hong, C.H.I. Ming, X.U. Xiang, Effect of mineral matter on product evolution during pyrolysis of Huadian oil shale, J. Fuel Chem. Technol. 44 (2016) 328–334.
[17] C. Rusi Zuo, Xiang Zeng, Zhongxiang, Diagenetic evolution and its significance of zeolites in sedimentary rocks, Gxinjiang Pet. Geol. 44 (2023) 543–553.
[18] F. Congli Wan, Qiang Jin, Baojun, Current research situation on hydrocarbon-generating evolution of volcanic minerals upon hydrocarbon source rocks, Pet. Geol. Recover. Effic. 8 (2001) 9–11.
[19] I.M.S. Anekwe, M. Chetty, L. Khotseng, S. Kiambi, L. Maharaj, B. Oboirien, Y. M. Isa, Stability, deactivation and regeneration study of a newly developed HZSM-5 and Ni-doped HZSM-5 zeolite catalysts for ethanol-to-hydrocarbon conversion, Catal. Commun. 186 (2023) 106802, https://doi.org/10.1016/j.catcom.2023.106802.
[20] E. Corrao, F. Salomone, E. Giglio, M. Castellino, S.M. Ronchetti, M. Armandi, R. Pirone, S. Bensaid, CO2 conversion into hydrocarbons via modified Fischer-Tropsch synthesis by using bulk iron catalysts combined with zeolites, Chem. Eng. Res. Des. 197 (2023) 449–465, https://doi.org/10.1016/j.cherd.2023.07.052.
[21] H. Hassan, B.H. Hameed, Green hydroxyapatite-zeolite catalyst derived from steel waste as an effective catalyst for the hydrocarbon production via co-catalytic pyrolysis of sugarcane bagasse and high-density polyethylene, Catal. Commun. 184 (2023) 106795, https://doi.org/10.1016/j.catcom.2023.106795.
[22] Wan Congli, Jin Qiang, Fan Baojun, Current research situation on hydrocarbon-generating evolution of volcanic minerals upon hydrocarbon source rocks, Pet. Geol. Recover. Effic. 8 (2001) 9–11.
[23] S. Zhu, H. Cui, Y. Jia, X. Zhu, H. Tong, L. Ma, Occurrence, composition, and origin of analcime in sedimentary rocks of non-marine petroliferous basins in China, Mar. Pet. Geol. 113 (2020) 104164, https://doi.org/10.1016/j.marpetgeo.2019.104164.
[24] W.X. Shifa, Zhu, Zhu Xiaomin, Zeolite diagenesis andits eontrol on petroleum reservoir quality of Permian in northwesternmargin of Junggar Basin, China, Seientia Sin. Terae. 41 (2011) 1602–1612, https://doi.org/10.1360/zd-2011-41-11-1602.
[25] Z.J. yang JIANG Yun, M.A. ZHAO Shan rong, Chang-qian, Characteristics of Rock-Forming Minerals of Analcime Phonolite in the Damxung Area, Qinghai-Tibet Plateau: Evidence for Primary Analcime, Earth Sci. 33 (2008) 320–328, http://www.earth-science.net//article/id/1698.
[26] Y. Zhang, S. Chen, Q. Meng, J. Yan, X. Pu, W. Han, The discovery of analcite in fine-grained sedimentary rocks of the second member of Kongdian Formation in Cangdong Sag, Huanghua depression: Implications for early digenetic environment, China Pet. Explor. 20 (2015) 37–43.
[27] L.J.M.A. Cong, W.A.N.G. Jian, P.A.N. Xiaohui, Chen Jun, Shang Liang, Origin and significance of "sweet spots" of analcites in shale oil reservoirs in Permian Lucaogou Formation, Jimsar Sag, Junggar Basin, Pet. Geol. Exp. 40 (2020) 596–603.
[28] F. Chen, Discovery and adsorption performanceof analcite ores in Ordos Basin, Ind. Miner. Process. 4 (2015) 13–16.
[29] P.T. Williams, H.M. Chishti, Two stage pyrolysis of oil shale using a zeolite catalyst, J. Anal. Appl. Pyrolysis 55 (2000) 217–234, https://doi.org/10.1016/S0165-2370(00)00071-1.
[30] H. Yuan, C. Li, R. Shan, J. Zhang, Y. Wu, Y. Chen, Recent developments on the zeolites catalyzed polyolefin plastics pyrolysis, Fuel Process. Technol. 238 (2022) 107531, https://doi.org/10.1016/j.fuproc.2022.107531.
[31] M. Zhang, B. Qin, W. Zhang, J. Zheng, J. Ma, Y. Du, R. Li, Hydrocracking of light diesel oil over catalysts with industrially modified Y zeolites, Catalysts 10 (2020) 1–12, https://doi.org/10.3390/catal10080815.
[32] Zhao Yuzhang, Zhihong Wang, A novel catalytic property of high silicon zeolite catalyst-the synergetic reaction of N-alkane cracking and olefin polymerization and its application, Acta Pet. Sin. 4 (1992) 47–54.
[33] J.F. Luhr, T.K. Kyser, Primary igneous analcime: the Colima minettes, Am. Mineral. 74 (1989) 216–223.
[34] R.R. Remy, R.E. Ferrell, Distribution and origin of analcime in marginal lacustrine mudstones of the Green River Formation, south-central Uinta basin, Utah, Clays Clay Min. 37 (1989) 419–432.
[35] R.W. RENAUT, Zeolitic diagenesis of late Ouaternary fluviolacustrine sediments and associatedcalcrete formation in the Lake Bogoria Basin, Kenya Rift Valley, Sedimentology 40 (1993) 271–301.
[36] R.L. HAY, Zeolites and zeolitic reactions in sedimentary rocks, Geol. Soc. Am. (1966), https://doi.org/10.1130/SPE85-p1.
[37] R.L. Hay, R.A. Sheppard, Occurrence of zeolites in sedimentary rocks: an overview, Rev. Mineral. Geochem. 45 (2001) 217–234, https://doi.org/10.2138/rmg.2001.45.6.
[38] M. Do Campo, C. del Papa, J. Jiménez-Millán, F. Nieto, Clay mineral assemblages and analcime formation in a Palaeogene fluvial-lacustrine sequence (Maíz Gordo Formation Palaeogen) from northwestern Argentina, Sediment. Geol. 201 (2007) 56–74, https://doi.org/10.1016/j.sedgeo.2007.04.007.
[39] N. Karakaya, M.Ç . Karakaya, A. Temel, Mineralogical and chemical properties and the origin of two types of analcime in SW Ankara, Turkey, Clays Clay Min. 61 (2013) 231–257, https://doi.org/10.1346/CCMN.2013.0610306.
[40] L.Y. Qun, L.L.I. Hong, L. Quan Sheng, Y. Rui, L.I. Wei, Z.H.O.U. Xiao-hu, J.I.A. O. Xin, L. Chuan, S. Qin, Lithology and origin analysis of sublacustrine hydrothermal deposits characterized by analcime, sanidine, dolomite, quartz, etc. in lucaogou formation, middle permian, Santanghu Basin, Northeast Xinjiang, China, Acta Sedimentol. Sin. 30 (2012) 205–218.
[41] X. ZHAO, X. PU, J. YAN, F. JIN, Z. SHI, G. CHAI, W. HAN, Y. LIU, W. JIANG, C. CHEN, W. ZHANG, Z. FANG, D. XIE, Cycles of fine-grained sedimentation and their influences on organic matter distribution in the second member of Paleogene Kongdian Formation in Cangdong Sag, Bohai Bay Basin, East China, Pet. Explor. Dev. 50 (2023) 534–546, https://doi.org/10.1016/S1876-3804(23)60408-2.
[42] R. Yang, X. Zhao, H. Li, C. Zhao, X. Pu, H. Liu, L. Fu, C. Li, Evolution characteristics of the upper Paleozoic source kitchen and its controlling effects on hydrocarbon accumulation in the Paleozoic petroleum system in Huanghua Depression, Bohai Bay Basin, China, J. Pet. Sci. Eng. 193 (2020) 107415, https://doi.org/10.1016/j.petrol.2020.107415.
[43] X. ZHAO, X. PU, W. JIANG, L. ZHOU, F. JIN, D. XIAO, L. FU, H. LI, An exploration breakthrough in Paleozoic petroleum system of Huanghua Depression in Dagang Oilfield and its significance, North China, Pet. Explor. Dev. 46 (2019) 651–663, https://doi.org/10.1016/S1876-3804(19)60224-7.
[44] F. JIN, X. WANG, H. LI, X. WU, L. FU, D. LOU, J. ZHANG, J. FENG, Formation of the primary petroleum reservoir in Wumaying inner buried-hill of Huanghua Depression, Bohai Bay Basin, China, Pet. Explor. Dev. 46 (2019) 543–552, https://doi.org/10.1016/S1876-3804(19)60034-0.
[45] L. Zhou, C. Chen, F. Yang, W. Han, Q. Guan, Micropore structure characteristics and quantitative characterization methods of lacustrine shale-A case study from the member 2 of Kongdian Formation, Cangdong sag, Bohai Bay Basin, Pet. Res. 5 (2020) 93–102, https://doi.org/10.1016/j.ptlrs.2020.01.001.
[46] W. Zhao, W.F. Tan, Quantitative and structural analysis of minerals in soil clay fractions developed under different climate zones in China by XRD with Rietveld method, and its implications for pedogenesis, Appl. Clay Sci. 162 (2018) 351–361, https://doi.org/10.1016/j.clay.2018.05.019.
[47] M.D. Lewan, M.J. Kotarba, Thermal-maturity limit for primary thermogenic-gas generation from humic coals as determined by hydrous pyrolysis, Am. Assoc. Pet. Geol. Bull. 98 (2014) 2581–2610, https://doi.org/10.1306/06021413204.

[48] N. Mahlstedt, B. Horsfield, V. Dieckmann, Second order reactions as a prelude to gas generation at high maturity, Org. Geochem. 39 (2008) 1125–1129, https://doi.org/10.1016/j.orggeochem.2008.04.011.
[49] N. Sun, T. Chen, J. Zhong, J. Gao, X. Shi, C. Xue, R. Swennen, Petrographic and geochemical characteristics of deep-lacustrine organic-rich mudstone and shale of the Upper Triassic Chang 7 member in the southern Ordos Basin, northern China: Implications for shale oil exploration, J. Asian Earth Sci. 227 (2022) 105118, https://doi.org/10.1016/j.jseaes.2022.105118.
[50] B. Liu, N. Mahlstedt, B. Horsfield, S. Tian, Q. Huo, Z. Wen, Z. Pan, Phase behavior and GOR evolution using a natural maturity series of lacustrine oil-prone shale: Implications from compositional modelling, Org. Geochem. 185 (2023) 104675, https://doi.org/10.1016/j.orggeochem.2023.104675.
[51] L. Burnaz, A. Kalmykov, S. Grohmann, G. Kalmykov, R. Littke, Geochemistry and organic petrology of organic-rich shales of the Upper Jurassic – Lower Cretaceous Bazhenov Horizon in the Frolov Region, West Siberian Basin: implications for the reconstruction of the organic matter origin and paleoredox conditions, Mar. Pet. Geol. 143 (2022) 105809, https://doi.org/10.1016/j.marpetgeo.2022.105809.
[52] G. Shanmugam, Significance of Coniferous Rain Forests and Related Organic Matter in Generating Commercial Quantities of Oil, Gippsland Basin, Australia, Am. Assoc. Pet. Geol. Bull. 69 (1985) 1241–1254, https://doi.org/10.1306/ad462bc3-16f7-11d7-8645000102c1865d.
[53] L. Ha, A. Shepp, W. Ridg, Occ currence of zeolit tes in sed dimentar ry rocks: an overview w, Rev. Lit. Arts Am. (2001).
[54] W. Wei, X. Zhu, M. He, M. Wang, X. Liu, Original sediment composition of the Lower Cretaceous lacustrine tight-oil mudstone and influences on diagenesis and organic matter content, the Erennaoer Sag in Erlian Basin, NE China, Mar. Pet. Geol. 94 (2018) 131–143, https://doi.org/10.1016/j.marpetgeo.2018.03.019.
[55] X. Wang, X. Wang, S. Pan, Q. Yang, S. Hou, Y. Jiao, W. Zhang, Occurrence of analcime in the middle Jurassic coal from the Dongsheng Coalfield, northeastern Ordos Basin, China, Int. J. Coal Geol. 196 (2018) 126–138, https://doi.org/10.1016/j.coal.2018.07.004.
[56] A.S. Pepper, P.J. Corvi, Simple kinetic models of petroleum formation. Part I: oil and gas generation from kerogen, Mar. Pet. Geol. 12 (1995) 291–319, https://doi.org/10.1016/0264-8172(95)98381-E.
[57] L.L. Fu, L.I. Shu Yuan, Lin Shing, Guo Shao HuiEffects of inorganic salts on the hydrocarbon generation from kerogens2002, 31, pp.15–20. https://doi.org/10.19700/j.0379-1726.2002.01.003..
[58] E. Tannenbaum, I.R. Kaplan, Low-Mr hydrocarbons generated during hydrous and dry pyrolysis of kerogen, Nature 317 (1985) 708–709, https://doi.org/10.1038/317708a0.
[59] P. Boulet, H.C. Greenwell, S. Stackhouse, P.V. Coveney, Recent advances in understanding the structure and reactivity of clays using electronic structure calculations, J. Mol. Struct. Theochem. 762 (2006) 33–48, https://doi.org/10.1016/j.theochem.2005.10.028.
[60] C.R. Reddy, Y.S. Bhat, G. Nagendrappa, B.S. Jai Prakash, Brønsted and Lewis acidity of modified montmorillonite clay catalysts determined by FT-IR spectroscopy, Catal. Today 141 (2009) 157–160, https://doi.org/10.1016/j.cattod.2008.04.004.
[61] J.W. Jurg, E. Eism, Petroleum hydrocarbons: generation from fatty acid, Science 80 (144) (1964) 1451–1452.
[62] J.E. Cooper, E.E. Bray, A postulated role of fatty acids in petroleum formation, Geochim. Cosmochim. Acta 27 (1963) 1113–1127, https://doi.org/10.1016/0016-7037(63)90093-0.